

**Chaos in Dirac Electron Optics: Emergence of a Relativistic Quantum Chimera**Hong-Ya Xu,<sup>1</sup> Guang-Lei Wang,<sup>1</sup> Liang Huang,<sup>2</sup> and Ying-Cheng Lai<sup>1,\*</sup><sup>1</sup>*School of Electrical, Computer, and Energy Engineering, Arizona State University, Tempe, Arizona 85287-5706, USA*<sup>2</sup>*School of Physical Science and Technology, and Key Laboratory for Magnetism and Magnetic Materials of MOE, Lanzhou University, Lanzhou, Gansu 730000, China*

(Received 2 January 2018; published 23 March 2018)

We uncover a remarkable quantum scattering phenomenon in two-dimensional Dirac material systems where the manifestations of both classically integrable and chaotic dynamics emerge simultaneously and are electrically controllable. The distinct relativistic quantum fingerprints associated with different electron spin states are due to a physical mechanism analogous to a chiroptical effect in the presence of degeneracy breaking. The phenomenon mimics a chimera state in classical complex dynamical systems but here in a relativistic quantum setting—henceforth the term “Dirac quantum chimera,” associated with which are physical phenomena with potentially significant applications such as enhancement of spin polarization, unusual coexisting quasibound states for distinct spin configurations, and spin selective caustics. Experimental observations of these phenomena are possible through, e.g., optical realizations of ballistic Dirac fermion systems.

DOI: [10.1103/PhysRevLett.120.124101](https://doi.org/10.1103/PhysRevLett.120.124101)

The tremendous development of two-dimensional (2D) Dirac materials such as graphene, silicene, and germanene [1–5], in which the low-energy excitations follow the relativistic energy-momentum relation and obey the Dirac equation, has led to the emergence of a new area of research: Dirac electron optics [6–33]. Theoretically, it was articulated early [7] that Klein tunneling and the unique gapless conical dispersion relation can be exploited to turn a simply *p-n* junction into a highly transparent focusing lens with a gate-controlled *negative refractive index*, producing a Veselago lens for the chiral Dirac fermions in graphene. The negative refraction of Dirac fermions obeys the Snell’s law in optics and the angularly resolved transmittances in analogy with the Fresnel coefficients in optics have been recently confirmed experimentally [20,26]. Other works include various Klein-tunneling junction based electronic counterparts of optical phenomena such as Fabry-Pérot resonances [8,13], cloaking [11,14], waveguides [12,19], the Goos-Hänchen effect [9], the Talbot effect [22], beam splitter and collimation [21,28,29], and even the Dirac fermion microscope [33]. A Dirac material based electrostatic potential junction with a closed interface can be effectively tuned to optical guiding and acts as an unusual quantum electron-optics element whose effective refractive index can be electrically modulated, in which phenomena such as gate controlled caustics [6], electron Mie scattering [15,23–25], and whispering gallery modes [17,18,30,31] can arise. In addition, unconventional electron optical elements have been demonstrated such as valley resolved waveguides [34,35] and beam splitters [27], electronic birefringent superlens [16], and spin (current) lens [10,32]. Research on Dirac electron

optics offers the possibility to control Dirac electron flows in a similar way as for light.

In this Letter, we address the role of chaos in Dirac electron optics. In nonrelativistic quantum mechanics, the interplay between chaos and quantum optics has been studied in microcavity lasers [36–39] and deformed dielectric microcavities with non-Hermitian physics and wave chaos [40]. With the development of Dirac electron optics [6–33], the relativistic electronic counterparts of deformed optical dielectric cavities or resonators have become accessible. For massless Dirac fermions in ballistic graphene, the interplay between classical dynamics and electrostatic confinement has been studied [41–44] with the finding that integrable dynamics lead to sharp transport resonances due to the emergence of bound states while chaos typically removes the resonances. In these works, the uncharged degree of freedom such as electron spin, which is fundamental to relativistic quantum systems, was not treated.

Our focus is on the interplay between ray-path defined classical dynamics and spin in Dirac electron optical systems. To be concrete, we introduce an electrical gate potential defined junction with a ring geometry, in analogy to a dielectric annular cavity. Classically, this system generates integrable and mixed dynamics with the chaotic fraction of the phase space depending on the ring eccentricity and the effective refractive index configuration, where the index can be electrically tuned to negative values to enable Klein tunneling. Inside the gated region, the electron spin degeneracy is lifted through an exchange field from induced ferromagnetism, leading to a class of spin-resolved, electrically tunable quantum systems of

electron optics with massless Dirac fermions (by mimicking the photon polarization resolved photonic cavities made from synthesized chiral metamaterials). We develop an analytic wave function matching solution scheme and uncover a striking quantum scattering phenomenon: manifestations of classically integrable and chaotic dynamics coexist simultaneously in the system at the same parameter setting, which mimics a chimera state in classical complex dynamical systems [45–52]. The basic underlying physics is the well-defined, spin-resolved, gate-controllable refraction index that dominantly controls the ballistic motion of short-wavelength Dirac electrons across the junction interface, in which the ray tracing of reflection and refraction associated with particles belonging to different spin states generates distinct classical dynamics inside the junction or scatterer. Especially, with a proper gate potential, the spin-dependent refractive index profile can be controlled to generate regular ray dynamics for one spin state but generically irregular behavior with chaos for the other. A number of highly unusual physical phenomena arise, such as enhanced spin polarization with chaos, simultaneous quasicarried and whispering gallery type of resonances, and spin-selective lensing with a starkly near-field separation between the local density of states (DOS) for spin-up and spin-down particles.

Low energy excitations in 2D Dirac materials are described by the Dirac-Weyl Hamiltonian  $H_0 = v_F \boldsymbol{\sigma} \cdot \mathbf{p}$ , where  $v_F$  is the Fermi velocity,  $\mathbf{p} = (p_x, p_y)$  is the momentum measured from a given Dirac point, and  $\boldsymbol{\sigma} = (\sigma_x, \sigma_y)$  are Pauli matrices for sublattice pseudospin. In the presence of a gate potential and an exchange field due to the locally induced ferromagnetism inside the whole gated region, the effective Hamiltonian is  $H = v_F s_0 \otimes \boldsymbol{\sigma} \cdot \mathbf{p} + s_0 \otimes \sigma_0 \mathcal{V}_{\text{gate}}(\mathbf{r}) - s_z \otimes \sigma_0 \mathcal{M}(\mathbf{r})$ , where the Pauli matrix  $s_z$  acts on the real electron spin space,  $s_0$  and  $\sigma_0$  both are identity matrices,  $\mathcal{V}_{\text{gate}}(\mathbf{r})$  and  $\mathcal{M}(\mathbf{r})$  are the electrostatic and exchange potential, respectively. Because of the pseudospin-momentum locking (i.e.,  $\boldsymbol{\sigma} \cdot \mathbf{p}$ ), a nonuniform potential couples the two pseudospinor components, but the electron spin components are not coupled with each other. The exchange field breaks the twofold spin degeneracy. Since  $[s_z \otimes \sigma_0, H] = 0$ , the Hamiltonian can be simplified as  $H_s = H_0 + \mathcal{V}_{\text{gate}}(\mathbf{r}) - s \mathcal{M}(\mathbf{r})$  with  $s = \pm$  denoting the electron spin quantum number. Because of  $\mathcal{M}$ , the Dirac-type Hamiltonian  $H_s$  can give rise to spin dependent physical processes.

For the ring configuration in Fig. 1(a) and assuming the potentials are smooth on the scale of the lattice spacing but sharp in comparison with the conducting carriers' wavelength, in the polar coordinates  $\mathbf{r} = (r, \theta)$ , we have  $\mathcal{V}_{\text{gate}}(\mathbf{r}) = \hbar v_F \nu_1 \Theta(R_1 - r) \Theta(|\mathbf{r} - \boldsymbol{\xi}| - R_2) + \hbar v_F \nu_2 \Theta(R_2 - |\mathbf{r} - \boldsymbol{\xi}|)$ , and  $\mathcal{M}(\mathbf{r}) = \hbar v_F \mu \Theta(R_1 - r)$ , where  $\Theta$  is the Heaviside step function,  $R_2$  is the radius of the small disk gated region of strength  $\hbar v_F (\nu_2 - \nu_1)$  placed inside a larger disk of radius  $R_1$  ( $> R_2$ ) and strength  $\hbar v_F \nu_1$ , the displacement vector between

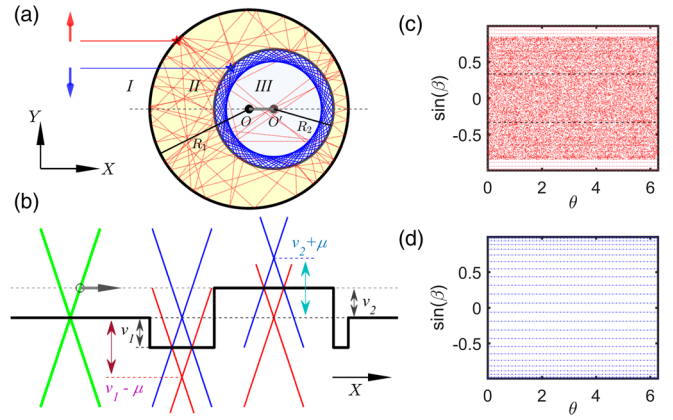


FIG. 1. Scattering system and classical ray dynamics. (a) Annular shaped scattering region with eccentricity  $\xi = OO'$ , (b) a cross-sectional view, (c), (d) chaotic and integrable ray dynamics on the Poincaré surface of section defined by the Birkhoff coordinates  $(\theta, \sin\beta)$  for spin-up and -down particles, respectively, where  $\theta$  denotes the polar angle of a ray's intersection point with the cavity boundary and  $\beta$  is the angle of incidence with respect to the boundary normal. The quantity  $\sin\beta$  is proportional to the angular momentum and the critical lines for total internal reflection are given by  $\sin\beta_c = \pm 1/n_s$ .

the disk centers is  $\boldsymbol{\xi} = (\xi, 0)$ , and the exchange potential has the strength  $\hbar v_F \mu$  over the whole gated region. The two circular boundaries divide the domain into three distinct regions: I:  $r > R_1$ ; II:  $r < R_1$  and  $|\mathbf{r} - \boldsymbol{\xi}| > R_2$ ; III:  $|\mathbf{r} - \boldsymbol{\xi}| < R_2$ . For given particle energy  $E = \hbar v_F \epsilon$ , the momenta in the respective regions are  $k_s^I = |\epsilon|$ ,  $k_s^{II} = |\epsilon - \nu_1 + s\mu|$ , and  $k_s^{III} = |\epsilon - \nu_2 + s\mu|$ . Within the gated region, the exchange potential splits the Dirac cone into two in the vertical direction in the energy domain while the electrostatic potential simply shifts the cone, leading to a spin-resolved, gate-controllable annular junction for massless Dirac electrons.

In the short wavelength limit, locally the curved junction interface appears straight for the electrons, so the gated regions and the surroundings can be treated as optical media. The unusual feature here is that the refractive indices are spin dependent:  $n_s^{II,III} = (\epsilon + s\mu - \nu_{1,2})/\epsilon$ , similar to light entering and through a polarization resolved photonic crystal [53,54]. Given the values of  $\epsilon$  and  $\mu$ , depending on the values of  $\nu_{1,2}$ , the refractive indices for the two spin states can be quite distinct with opposite signs. The system is thus analogous to a chiral photonic metamaterial based cavity, which represents a novel class of Dirac electron optics systems.

The classical behaviors of Dirac-like particles in the short wavelength limit can be assessed using the optical analogy, as done previously for circularly curved  $p$ - $n$  junctions [6,33], where the classical trajectories are defined via the principle of least time. Because of the spin dependent and piecewise constant nature of the index profile, the resulting stationary ray paths for the Dirac

electrons are spin-resolved and consist of straight line segments. At a junction interface, there is ray splitting governed by the spin-resolved Snell's law. On a Poincaré surface of the section, the classical dynamics are described by a spin-resolved map  $F_s$  relating the dynamical variables  $\theta$  and  $\beta$  (Fig. 1) between two successive collisions with the interface:  $(\theta_i, \sin \beta_i) \mapsto (\theta_{i+1}, \sin \beta_{i+1})$ . The ray-splitting picture is adequate for uncovering the relativistic quantum fingerprints of distinct classical dynamics.

Spin-resolved ray trajectories inside the junction lead to the simultaneous coexistence of distinct classical dynamics. For example, for the parameter setting  $\nu_2 = -\nu_1 = \epsilon = \mu$ , i.e.,  $n_s^{\text{II}} = 2 + s$  and  $n_s^{\text{III}} = s$ , for spin-up particles ( $s = +$ ), the junction is an eccentric annular electron cavity characterized by the refractive indices  $n_+^{\text{II}} = 3$  and  $n_+^{\text{III}} = 1$ , as exemplified in Fig. 1(b) for  $\xi = 0.3$ . However, for spin-down particles ( $s = -$ ), the junction appears as an off-centered negatively refracted circular cavity with  $n_-^{\text{II}} = 1$  and  $n_-^{\text{III}} = -1$ . Figures 1(c) and 1(d) show the corresponding ray dynamics on the Poincaré surface of section for spin-up and -down particles, respectively, where the former exhibit chaos while the dynamics associated with the latter are integrable with angular momentum being the second constant of motion.

For a spin unpolarized incident beam, the simultaneous occurrence of integrable and chaotic classical dynamics means the coexistence of distinct quantum manifestations, leading to the emergence of a Dirac quantum chimera. To establish this, we carry out a detailed analysis of the scattering matrices for spin-dependent, relativistic quantum scattering and transport through the junction. Using insights from analyzing optical dielectric cavities [55,56] and nonrelativistic quantum billiard systems [57,58], we develop an analytic wave function matching scheme at the junction interfaces (See Supplemental Material [59] which includes Refs. [24,30,60–64]) to solve the Dirac-Weyl equation to obtain the scattering matrix  $S$  as a function of the energy  $E$  as well as the spin polarization  $s$  for given system parameters  $R_2/R_1$ ,  $\xi$ ,  $\nu_{1,2}$ , and  $\mu$ . The Wigner-Smith time delay [60,61] is defined from the  $S$  matrix as  $\tau = -i\hbar \text{Tr}[S^\dagger (\partial S / \partial E)]$ , which is proportional to the DOS of the cavity. Large positive values of  $\tau$  signify resonances associated with the quasibound states [65]. Physically, a sharper resonance corresponds to a longer trapping lifetime and scattering time delay. Previous works on wave or quantum chaotic scattering [66–85] established that classical chaos can smooth out (broaden) the sharp resonances and reduce the time delay markedly while integrable dynamics can lead to stable, long-lived bound states (or trapping modes).

We present concrete evidence for Dirac quantum chimera. Figure 2(a) shows, for  $R_2/R_1 = 0.6$ ,  $\mu = -\nu_1 = 5$ , and  $\nu_2 = 45$ , the dimensionless time delay (on a logarithmic scale) versus the eccentricity  $\xi$  and energy  $E$  (in units of  $\hbar v_F/R_1$ ). Figure 2(b) shows the maximum time delay

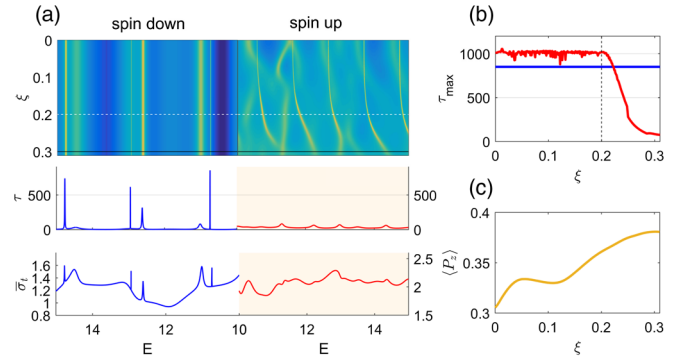


FIG. 2. A Dirac quantum chimera. (a) Top: Contour map of dimensionless Wigner-Smith time delay (on a logarithmic scale) versus energy  $E$  and eccentricity  $\xi$  for spin-down (left) and -up (right) cases, where the bright yellow color indicates larger values. Middle and bottom panels: time delay and total cross section averaged over all directions of the incident waves versus  $E$ , respectively, for  $\xi = 0.3$ . (b) Dependence of the maximum time delay on  $\xi$  (red: spin-up; blue: spin-down). (c) Energy averaged spin polarization versus  $\xi$ .

[within the given energy range in Fig. 2(a)] versus  $\xi$  for spin-up (red) and spin-down (blue) particles. There are drastic changes in the time delay as the energy is varied, which are characteristic of well-isolated, narrow resonances and imply the existence of relatively long-lived confined modes. There is a key difference in the resonances associated with the spin-up and -down states: the former depend on the eccentricity parameter  $\xi$  and are greatly suppressed for  $\xi > 0.2$ , while the latter are independent of  $\xi$ . For example, the middle panel of Fig. 2(a) shows that, for a severely deformed structure ( $\xi = 0.3$ ), there are sharp resonances with high peak values of the time delay for the spin down state, but none for the spin-up state. The suppression of resonances associated with the spin-up state is consistent with the behavior of the total cross section  $\bar{\sigma}_t$  (averaged over the directions of the incident wave) given in terms of the  $S$ -matrix elements by  $\bar{\sigma}_t = (2k)^{-1} \sum_{m,l=-\infty}^{\infty} |S_{ml} - \delta_{ml}|^2$ , as shown in the bottom panel of Fig. 2(a). Because the classical dynamics for massless fermions in the spin-up and -down states are chaotic and integrable, respectively [cf., Figs. 1(c), 1(d)], there is *simultaneous* occurrence of two characteristically different quantum scattering behaviors for a spin unpolarized beam: one without and another with *sharp* resonances. This striking contrast signifies a Dirac quantum chimera.

Are there unexpected, counterintuitive physical phenomena associated with a Dirac quantum chimera? Yes, there are. Here we present two and point out their applied values.

The first is spin polarization enhancement, which has potential applications to Dirac material based spintronics. A general way to define spin polarization is through the spin conductivities  $G^{\downarrow(\uparrow)}$  as  $P_z = (G^\downarrow - G^\uparrow)/(G^\downarrow + G^\uparrow)$ . Imagine a system consisting of a set of sparse, randomly distributed, identical junction-type of annular scatterers,

and assume that the scatterer concentration is sufficiently low ( $n_c \ll 1/R_1^2$ ) so that multiple scattering events can be neglected. In this case, the spin conductivities can be related to the transport cross section as  $G^{\downarrow(\uparrow)}/G_0 = k/(n_c \sigma_{\text{tr}}^{\downarrow(\uparrow)})$ , where  $G_0$  is the conductance quantum and  $\sigma_{\text{tr}}^{\downarrow(\uparrow)}$  can be calculated from the  $S$  matrix. For a spin unpolarized incident beam along the  $x$  axis with equal spin-up and -down populations, we calculate the average spin polarization over a reasonable Fermi energy range as a function of the eccentricity  $\xi$ , as shown in Fig. 2(c). For  $\xi > 0.2$  so classical chaos is relatively well developed and a Dirac quantum chimera emerges, there is robust enhancement of spin polarization. From the standpoint of classical dynamics, the scattering angle is much more widely distributed for spin-up particles (due to chaos) as compared with the angle distribution for spin-down particles with integrable dynamics, leading to a larger effective resistance for spin-up particles. From an applied perspective, the enhancement of spin polarization brought about by a Dirac quantum chimera can be exploited for developing spin rheostats or filters, where one of the spin resistances, e.g.,  $R^\uparrow \propto 1/G^\uparrow$ , can be effectively modulated through tuning the deformation parameter  $\xi$  so as to induce classically

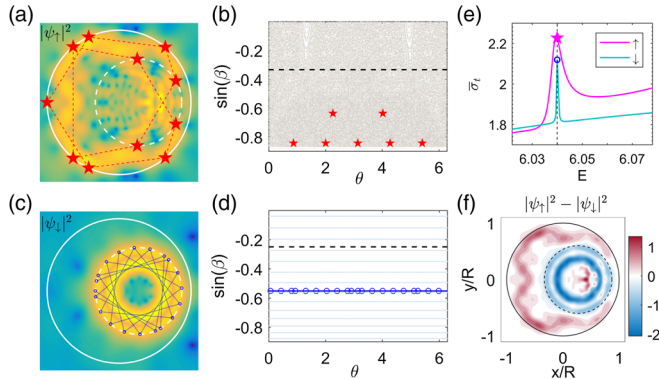


FIG. 3. Spin polarized scarred and regular whispering-gallery-mode resonances as a result of Dirac quantum chimera. (a), (c) Real space probability densities (on a logarithmic scale) of the representative quasibound states for spin-up and spin-down Dirac electrons, respectively. For the spin-up particles, the spinor wave solution is scarred by an unstable periodic ray trajectory obeying the Snell's law, as indicated by the red-dashed path with highlighted pentagram markers. The spin-down Dirac electrons are associated with a whispering gallery ray path due to the continuous total internal reflections denoted by the blue dotted segments. (b), (d) The corresponding phase-space representations with regions below the critical black dashed lines satisfying the total internal reflection at the boundary. The distinct quasibound modes are from simultaneous resonances under the same system parameters, leading to a relativistic quantum chimera. Further signatures of the chimera state can be seen in the plot of the total cross section versus the particle energy for different spin states (e) and a net spin distribution with a dramatic spin-resolved separation in the real space confined inside the cavity (f).

chaotic motion for one type of polarization but integrable dynamics for another.

The second phenomenon is resonance and lensing associated with a Dirac quantum chimera. Figures 3(a)–3(f) show, for  $\xi = 0.27$  (in units of  $R_1$ ),  $R_2/R_1 = 0.6$ ,  $\nu_2 = 4\nu_1 = -4\mu = 24.16$  (in units of  $1/R_1$ ) and  $E = 6.04$  (in units of  $\hbar v_F/R_1$ ), a resonant (quasibound) state, in which the spatially separated, spin-resolved local DOS is confined inside the cavity. The spin-up state is concentrated about a particular unstable periodic orbit without the rotational symmetry [Figs. 3(a) and 3(b)] and exhibits a scarring pattern with a relatively short lifetime characterized by a wider resonance profile, as shown in Fig. 3(e). Spin-down particles are trapped inside the inner disk by a regular long-lived whispering gallery mode associated with the integrable dynamics [Figs. 3(c) and 3(d)]. The Dirac quantum chimera thus manifests itself as the simultaneous occurrence of a magnetic scarred quasibound state and a whispering gallery mode excited by an incident wave with equal populations of spin-up and -down particles, as shown in Fig. 3(f), a color-coded spatial distribution of the difference between the local DOS for spin-up and -down particles.

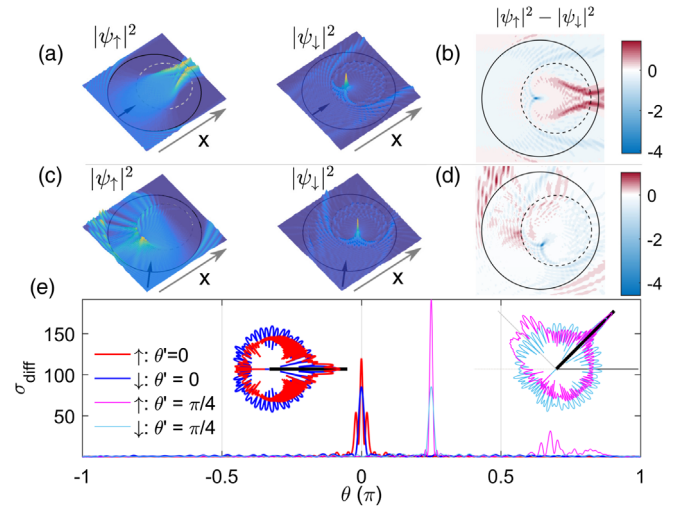


FIG. 4. Spin-selective caustic lens and skew scattering associated with a Dirac quantum chimera. (a) Caustic patterns resulting from the scattering of a spin unpolarized planar incident wave traveling along the positive  $x$  axis ( $\theta' = 0$ ) with relatively short wavelength, i.e.,  $kR_1 = 70 \gg 1$ , and (c) from scattering of the wave propagating along the direction that makes an angle  $\theta' = \pi/4$  with the  $x$  axis. (b), (d) The corresponding spatially resolved near field net spin distributions measured by the difference  $|\psi_\uparrow|^2 - |\psi_\downarrow|^2$ , respectively. (e) The resulting far-field behavior characterized by the angular distributions of spin-dependent differential cross sections with symmetric profiles for  $\theta' = 0$  (left inset) and a spin-selective asymmetric one for  $\theta' = \pi/4$  (right inset), where both insets are plotted by the eighth root of  $\sigma_{\text{diff}}^{\uparrow(\downarrow)}$  in order to weaken the drastic contrast variation in magnitude for better visualization. Parameters are  $\xi = 0.27$ ,  $R_2/R_1 = 0.6$ ,  $\nu_2 = \mu = -\nu_1 = 70$ , and  $E = 70$ .

In the sufficiently short wavelength regime where the ray picture becomes accurate, a spin-resolved lensing behavior arises, due to the simultaneous occurrence of two distinct quantum states associated with the chimera state. The cavity can be regarded as an effective electronic Veselago lens with a robust caustic function for spin-down particles but the spin-up particles encounter simply a conventional lens of an irregular shape. Particularly, for a spin-unpolarized, planar incident wave, a spin-selective caustic behavior arises, as shown in Figs. 4(a)–4(d) through the color-coded near-field patterns. There is a pronounced lensing caustic of the cusp type for the spin-down state while a qualitatively distinct lensing pattern occurs for the spin-up state. A consistent far-field angular distribution of the differential cross section is shown in Fig. 4(e), which gives rise to well-oriented or -collimated, spin-dependent far-field scattering with the angle resolved profile minimized into a small range due to the lensing effect. Despite a lack of robust lensing, the spin-up particles in general undergo asymmetric scattering, which can lead to spin-polarized transverse transport in addition to longitudinal spin filtering.

To summarize, we uncover a Dirac quantum chimera—a type of relativistic quantum scattering states characterized by the simultaneous coexistence of two distinct types of behaviors as the manifestations of classical chaotic and integrable dynamics, respectively. The physical origin of the chimera state is the optical-like behavior of massless Dirac fermions with both spin and pseudospin degrees of freedom, which together define a spin-resolved Snell's law governing the chiral particles' ballistic motion. The phenomenon is predicted analytically based on quantum scattering from a gate-defined annular junction structure. The chimera has striking physical consequences such as spin polarization enhancement, unusual quantum resonances, and spin-selective lensing, which are potentially exploitable for developing 2D Dirac material-based electronic and spintronic devices.

We would like to acknowledge support from the Vannevar Bush Faculty Fellowship program sponsored by the Basic Research Office of the Assistant Secretary of Defense for Research and Engineering and funded by the Office of Naval Research through Grant No. N00014-16-1-2828. L. H. is also supported by NNSF of China under Grant No. 11775101.

---

\*Ying-Cheng.Lai@asu.edu

- [1] K. S. Novoselov, A. K. Geim, S. V. Morozov, D. Jiang, Y. Zhang, S. V. Dubonos, I. V. Grigorieva, and A. A. Firsov, *Science* **306**, 666 (2004).
- [2] K. S. Novoselov, A. K. Geim, S. V. Morozov, D. Jiang, M. I. Katsnelson, I. V. Grigorieva, S. V. Dubonos, and A. A. Firsov, *Nature (London)* **438**, 197 (2005).
- [3] A. H. C. Neto, F. Guinea, N. M. R. Peres, K. S. Novoselov, and A. K. Geim, *Rev. Mod. Phys.* **81**, 109 (2009).
- [4] T. Wehling, A. Black-Schaffer, and A. Balatsky, *Adv. Phys.* **63**, 1 (2014).
- [5] J. Wang, S. Deng, Z. Liu, and Z. Liu, *Nat. Sci. Rev.* **2**, 22 (2015).
- [6] J. Cserti, A. Pályi, and C. Péterfalvi, *Phys. Rev. Lett.* **99**, 246801 (2007).
- [7] V. V. Cheianov, V. Fal'ko, and B. L. Altshuler, *Science* **315**, 1252 (2007).
- [8] A. V. Shytov, M. S. Rudner, and L. S. Levitov, *Phys. Rev. Lett.* **101**, 156804 (2008).
- [9] C. W. J. Beenakker, R. A. Sepkhanov, A. R. Akhmerov, and J. Tworzydło, *Phys. Rev. Lett.* **102**, 146804 (2009).
- [10] A. G. Moghaddam and M. Zareyan, *Phys. Rev. Lett.* **105**, 146803 (2010).
- [11] N. Gu, M. Rudner, and L. Levitov, *Phys. Rev. Lett.* **107**, 156603 (2011).
- [12] J. R. Williams, T. Low, M. S. Lundstrom, and C. M. Marcus, *Nat. Nanotechnol.* **6**, 222 (2011).
- [13] P. Rickhaus, R. Maurand, M.-H. Liu, M. Weiss, K. Richter, and C. Schönenberger, *Nat. Commun.* **4**, 2342 (2013).
- [14] B. Liao, M. Zebarjadi, K. Esfarjani, and G. Chen, *Phys. Rev. B* **88**, 155432 (2013).
- [15] R. L. Heinisch, F. X. Bronold, and H. Fehske, *Phys. Rev. B* **87**, 155409 (2013).
- [16] M. M. Asmar and S. E. Ulloa, *Phys. Rev. B* **87**, 075420 (2013).
- [17] J.-S. Wu and M. M. Fogler, *Phys. Rev. B* **90**, 235402 (2014).
- [18] Y. Zhao, J. Wyrick, F. D. Natterer, J. F. Rodriguez-Nieva, C. Lewandowski, K. Watanabe, T. Taniguchi, L. S. Levitov, N. B. Zhitenev, and J. A. Stroscio, *Science* **348**, 672 (2015).
- [19] P. Rickhaus, M.-H. Liu, P. Makk, R. Maurand, S. Hess, S. Zihlmann, M. Weiss, K. Richter, and C. Schonenberger, *Nano Lett.* **15**, 5819 (2015).
- [20] G.-H. Lee, G.-H. Park, and H.-J. Lee, *Nat. Phys.* **11**, 925 (2015), letter.
- [21] P. Rickhaus, P. Makk, K. Richter, and C. Schonenberger, *Appl. Phys. Lett.* **107**, 251901 (2015).
- [22] J. D. Walls and D. Hadad, *Sci. Rep.* **6**, 26698 (2016).
- [23] J. Caridad, S. Connaughton, C. Ott, H. B. Weber, and V. Krstic, *Nat. Commun.* **7**, 12894 (2016).
- [24] C. Gutierrez, L. Brown, C.-J. Kim, J. Park, and A. N. Pasupathy, *Nat. Phys.* **12**, 1069 (2016).
- [25] J. Lee, D. Wong, J. Velasco Jr., J. F. Rodriguez-Nieva, S. Kahn, H.-Z. Tsai, T. Taniguchi, K. Watanabe, A. Zettl, F. Wang, L. S. Levitov, and M. F. Crommie, *Nat. Phys.* **12**, 1032 (2016).
- [26] S. Chen, Z. Han, M. M. Elahi, K. M. M. Habib, L. Wang, B. Wen, Y. Gao, T. Taniguchi, K. Watanabe, J. Hone, A. W. Ghosh, and C. R. Dean, *Science* **353**, 1522 (2016).
- [27] M. Settnes, S. R. Power, M. Brandbyge, and A.-P. Jauho, *Phys. Rev. Lett.* **117**, 276801 (2016).
- [28] M.-H. Liu, C. Gorini, and K. Richter, *Phys. Rev. Lett.* **118**, 066801 (2017).
- [29] A. W. Barnard, A. Hughes, A. L. Sharpe, K. Watanabe, T. Taniguchi, and D. Goldhaber-Gordon, *Nat. Commun.* **8**, 15418 (2017).

- [30] Y. Jiang, J. Mao, D. Moldovan, M. R. Masir, G. Li, K. Watanabe, T. Taniguchi, F. M. Peeters, and E. Y. Andrei, *Nat. Nanotechnol.* **12**, 1045 (2017).
- [31] F. Ghahari, D. Walkup, C. Gutiérrez, J. F. Rodríguez-Nieva, Y. Zhao, J. Wyrick, F. D. Natterer, W. G. Cullen, K. Watanabe, T. Taniguchi, L. S. Levitov, N. B. Zhitenev, and J. A. Stroschio, *Science* **356**, 845 (2017).
- [32] S.-H. Zhang, J.-J. Zhu, W. Yang, and K. Chang, *2D Mater.* **4**, 035005 (2017).
- [33] P. Bäggi, J. M. Caridad, C. Stampfer, G. Calogero, N. R. Papior, and M. Brandbyge, *Nat. Commun.* **8**, 15783 (2017).
- [34] Z. Wu, F. Zhai, F. M. Peeters, H. Q. Xu, and K. Chang, *Phys. Rev. Lett.* **106**, 176802 (2011).
- [35] F. Zhai, Y.-L. Ma, and K. Chang, *New J. Phys.* **13**, 083029 (2011).
- [36] J. U. Nöckel, A. D. Stone, G. Chen, H. L. Grossman, and R. K. Chang, *Opt. Lett.* **21**, 1609 (1996).
- [37] J. U. Nöckel and A. D. Stone, *Nature (London)* **385**, 45 (1997).
- [38] C. Gmachl, F. Capasso, E. E. Narimanov, J. U. Nöckel, A. D. Stone, J. Faist, D. L. Sivco, and A. Y. Cho, *Science* **280**, 1556 (1998).
- [39] K. J. Vahala, *Nature (London)* **424**, 839 (2003).
- [40] H. Cao and J. Wiersig, *Rev. Mod. Phys.* **87**, 61 (2015).
- [41] J. H. Bardarson, M. Titov, and P. W. Brouwer, *Phys. Rev. Lett.* **102**, 226803 (2009).
- [42] M. Schneider and P. W. Brouwer, *Phys. Rev. B* **84**, 115440 (2011).
- [43] J. Heintl, M. Schneider, and P. W. Brouwer, *Phys. Rev. B* **87**, 245426 (2013).
- [44] M. Schneider and P. W. Brouwer, *Phys. Rev. B* **89**, 205437 (2014).
- [45] Y. Kuramoto and D. Battogtokh, *Nonlinear Phenom. Complex Syst.* **5**, 380 (2002).
- [46] D. M. Abrams and S. H. Strogatz, *Phys. Rev. Lett.* **93**, 174102 (2004).
- [47] D. M. Abrams and S. H. Strogatz, *Int. J. Bifurcation Chaos Appl. Sci. Eng.* **16**, 21 (2006).
- [48] M. R. Tinsley, S. Nkomo, and K. Showalter, *Nat. Phys.* **8**, 662 (2012).
- [49] A. M. Hagerstrom, T. E. Murphy, R. Roy, P. Hövel, I. Omelchenko, and E. Schöll, *Nat. Phys.* **8**, 658 (2012).
- [50] E. A. Martens, S. Thutupalli, A. Fourrière, and O. Hallatschek, *Proc. Natl. Acad. Sci. U.S.A.* **110**, 10563 (2013).
- [51] N. Yao, Z.-G. Huang, Y.-C. Lai, and Z.-G. Zheng, *Sci. Rep.* **3**, 3522 (2013).
- [52] N. Yao, Z.-G. Huang, C. Grebogi, and Y.-C. Lai, *Sci. Rep.* **5**, 12988 (2015).
- [53] J. K. Gansel, M. Thiel, M. S. Rill, M. Decker, K. Bade, V. Saile, G. von Freymann, S. Linden, and M. Wegener, *Science* **325**, 1513 (2009).
- [54] S. Zhang, Y.-S. Park, J. Li, X. Lu, W. Zhang, and X. Zhang, *Phys. Rev. Lett.* **102**, 023901 (2009).
- [55] G. Hackenbroich and J. U. Nöckel, *Europhys. Lett.* **39**, 371 (1997).
- [56] M. Hentschel and K. Richter, *Phys. Rev. E* **66**, 056207 (2002).
- [57] E. Doron and U. Smilansky, *Nonlinearity* **5**, 1055 (1992).
- [58] E. Doron and S. D. Frisch, *Phys. Rev. Lett.* **75**, 3661 (1995).
- [59] See Supplemental Material at <http://link.aps.org/supplemental/10.1103/PhysRevLett.120.124101> for a detailed analytical derivation of the scattering matrix for the Dirac electron optical system with classically integrable or chaotic dynamics. Formulas for various characterizing quantities (e.g., scattering cross sections) and numerical validation are also included.
- [60] E. P. Wigner, *Phys. Rev.* **98**, 145 (1955).
- [61] F. T. Smith, *Phys. Rev.* **118**, 349 (1960).
- [62] H. Schomerus, M. Marciiani, and C. W. J. Beenakker, *Phys. Rev. Lett.* **114**, 166803 (2015).
- [63] D. Zwillinger, *Table of Integrals, Series, and Products* (Elsevier Science, New York, 2014).
- [64] P. Wei, S.-W. Lee, F. Lemaitre, L. Pinel, D. Cutaia, W.-J. Cha, F. Katmis, Y. Zhu, D. Heiman, J. Hone, and J. S. M. C. -T. Chen, *Nat. Mater.* **15**, 711 (2016).
- [65] S. Rotter and S. Gigan, *Rev. Mod. Phys.* **89**, 015005 (2017).
- [66] R. Blümel and U. Smilansky, *Phys. Rev. Lett.* **60**, 477 (1988).
- [67] R. Blümel and U. Smilansky, *Physica (Amsterdam)* **36D**, 111 (1989).
- [68] R. A. Jalabert, H. U. Baranger, and A. D. Stone, *Phys. Rev. Lett.* **65**, 2442 (1990).
- [69] C. M. Marcus, A. J. Rimberg, R. M. Westervelt, P. F. Hopkins, and A. C. Gossard, *Phys. Rev. Lett.* **69**, 506 (1992).
- [70] Y.-C. Lai, R. Blümel, E. Ott, and C. Grebogi, *Phys. Rev. Lett.* **68**, 3491 (1992).
- [71] R. Ketzmerick, *Phys. Rev. B* **54**, 10841 (1996).
- [72] T. Kottos and U. Smilansky, *Phys. Rev. Lett.* **79**, 4794 (1997).
- [73] A. S. Sachrajda, R. Ketzmerick, C. Gould, Y. Feng, P. J. Kelly, A. Delage, and Z. Wasilewski, *Phys. Rev. Lett.* **80**, 1948 (1998).
- [74] T. Kottos, U. Smilansky, J. Fortuny, and G. Nesti, *Radio Sci.* **34**, 747 (1999).
- [75] T. Kottos and U. Smilansky, *Phys. Rev. Lett.* **85**, 968 (2000).
- [76] B. Huckestein, R. Ketzmerick, and C. H. Lewenkopf, *Phys. Rev. Lett.* **84**, 5504 (2000).
- [77] G. Casati, I. Guarneri, and G. Maspero, *Phys. Rev. Lett.* **84**, 63 (2000).
- [78] A. P. S. de Moura, Y.-C. Lai, R. Akis, J. P. Bird, and D. K. Ferry, *Phys. Rev. Lett.* **88**, 236804 (2002).
- [79] R. Crook, C. G. Smith, A. C. Graham, I. Farrer, H. E. Beere, and D. A. Ritchie, *Phys. Rev. Lett.* **91**, 246803 (2003).
- [80] T. Kottos and U. Smilansky, *J. Phys. A* **36**, 3501 (2003).
- [81] S. Gnuzmann and U. Smilansky, *Adv. Phys.* **55**, 527 (2006).
- [82] R. Band, A. Sawicki, and U. Smilansky, *J. Phys. A* **43**, 415201 (2010).
- [83] Y. Krivolapov, S. Fishman, E. Ott, and T. M. Antonsen, *Phys. Rev. E* **83**, 016204 (2011).
- [84] R. Yang, L. Huang, Y.-C. Lai, and C. Grebogi, *Europhys. Lett.* **94**, 40004 (2011).
- [85] G. L. Wang, L. Ying, Y.-C. Lai, and C. Grebogi, *Phys. Rev. E* **87**, 052908 (2013).

Supplementary Information for  
**Chaos in Dirac electron optics: Emergence of a relativistic quantum chimera**

Hong-Ya Xu, Guang-Lei Wang, Liang Huang, and Ying-Cheng Lai

Corresponding author: Y.-C. Lai (Ying-Cheng.Lai@asu.edu)

**CONTENTS**

I. Basics	1
II. Multichannel elastic scattering theory for two-dimensional massless Dirac fermions - $S$ -matrix approach	2
III. $S$ -matrix for <i>eccentric</i> annular shaped (ring) scatterer	6
IV. Calculation of wavefunctions	7
V. Ideal centric case: analytic results	8
VI. Validation of the $S$ -matrix approach	10
A. Symmetry constraints	10
B. The case of $\xi \rightarrow 0$	12
VII. Full data set for the plot Fig. 2(c) in the main text	12
VIII. Feasibility of experimental implementation	13
References	14

**I. BASICS**

The starting point of our analysis is the effective low-energy Hamiltonian of graphene or graphene-like systems with Dirac cones:

$$H = v_F s_0 \otimes \boldsymbol{\sigma} \cdot \mathbf{p} + s_0 \otimes \boldsymbol{\sigma}_0 \mathcal{V}_{gate}(\mathbf{r}) - s_z \otimes \boldsymbol{\sigma}_0 \mathcal{M}(\mathbf{r}), \quad (\text{S1.1})$$

where the identity matrix  $s_0$  and the Pauli matrix  $s_z$  act on the real electron spin space while the Pauli matrices  $\boldsymbol{\sigma} = (\boldsymbol{\sigma}_x, \boldsymbol{\sigma}_y)$  and the identity matrix  $\boldsymbol{\sigma}_0$  define the sublattice pseudospin. The first term in Eq. (S1.1) characterizes the pristine Dirac cone band dispersion with a four-fold degeneracy at a Dirac point: two for the sublattice pseudospin and two for the real electron spin. Since  $[s_z \otimes \boldsymbol{\sigma}_0, H] = 0$ , it is equivalent to two copies of Dirac-like Hamiltonian indexed by the spin quantum number  $s = \pm$ :

$$H_s = H_0 + \mathcal{V}_{gate}(\mathbf{r}) - s \mathcal{M}(\mathbf{r}), \quad (\text{S1.2})$$

where  $H_0 = v_F \boldsymbol{\sigma} \cdot \mathbf{p}$  is effectively the fundamental Dirac-Weyl Hamiltonian describing the two-dimensional free-space massless Dirac fermions. The Hamiltonian  $H_s$  acts on two-component pseudospinor waves for the massless Dirac quasiparticles belonging to the real spin state  $s$  in graphene or similar materials. The last two terms in Eq. (S1.1) represent the applied gate and exchange potential, respectively.

In the main text, the calculations are for the scattering of such quasiparticles from the step potential that can lead to spin-resolved ray-path defined classical dynamics in the short wavelength limit. The scattering process is of the relativistic type for massless Dirac fermions. In the following Secs. II-V, we develop an  $S$ -matrix based scheme to solve the relativistic quantum scattering problem, which is validated computationally in Sec. VI. In Sec. VII, we provide a detailed demonstration of the phenomenon of enhanced spin polarization as shown in Fig. 2(c) in the main text.

## II. MULTICHANNEL ELASTIC SCATTERING THEORY FOR TWO-DIMENSIONAL MASSLESS DIRAC FERMIONS - $S$ -MATRIX APPROACH

The main theoretical tool that we employ to investigate the role of chaos in Dirac electron optics is the formalism of stationary quantum scattering for two-dimensional massless Dirac fermions, where the scatterer has an irregular shape and a finite range. The scattering process is assumed to be elastic. The fundamental quantity of interest is the scattering ( $S$ -) matrix, from which all physically relevant quantities characterizing the scattering process can be deduced.

In the free space, the system is governed by the stationary Dirac-Weyl equation

$$H_0 \chi = \hbar v_F \boldsymbol{\sigma} \cdot \mathbf{k} \chi = E \chi, \quad (\text{S2.3})$$

for which the plane-wave solutions for energy  $E = \alpha \hbar v_F k$  is given by

$$\chi_k(\mathbf{r}) = \frac{1}{\sqrt{2}} \begin{pmatrix} 1 \\ \alpha e^{i\theta_k} \end{pmatrix} e^{i\mathbf{k} \cdot \mathbf{r}}, \quad (\text{S2.4})$$

where  $k = \sqrt{k_x^2 + k_y^2}$ ,  $\alpha = \text{sgn}(E)$  and  $\theta_k = \arctan(k_y/k_x)$  characterize the propagating direction parallel to the wavevector  $\mathbf{k}$  for  $E > 0$ . For  $E < 0$ , the two directions are anti-parallel with each other. In the polar coordinates  $\mathbf{r} = r(\cos \theta, \sin \theta)$ , the corresponding spinor cylindrical waves with given angular momentum and energy are

$${}^k h_m(r, \theta) = \begin{pmatrix} Z_m(kr) \\ i\alpha Z_{m+1}(kr) e^{i\theta} \end{pmatrix} e^{im\theta}, \quad (\text{S2.5})$$

where  $Z_m$  is the  $m$ -th order Bessel or Hankel function of the physically relevant kind. In particular, under the time convention  $e^{-iE/\hbar t}$  and for positive energy  $E > 0$ , we have

$${}^k h_m^{(-)} = \begin{pmatrix} H_m^{(2)}(kr) \\ iH_{m+1}^{(2)}(kr) e^{i\theta} \end{pmatrix} e^{im\theta}, \quad (\text{S2.6a})$$

as the cylindrical wave basis of the spinor waves of the incoming type, and

$${}^k h_m^{(+)} = \begin{pmatrix} H_m^{(1)}(kr) \\ iH_{m+1}^{(1)}(kr) e^{i\theta} \end{pmatrix} e^{im\theta}, \quad (\text{S2.6b})$$

as the outgoing type, where  $H_m^{(1)}$  and  $H_m^{(2)}$  denote the Hankel functions of the first and second kind, respectively.

For the scattering problem illustrated in Fig. 1 in the main text, the stationary wavefunction outside the scatterer generally can be decomposed into two parts - incoming and outgoing waves:

$$\Psi = \Psi_{in} + \Psi_{out}. \quad (\text{S2.7})$$

In the spinor cylindrical wave basis for massless Dirac fermions with positive energy, the incoming wave can be written as

$$\Psi_{in} = \sum_m a_m {}^k h_m^{(-)}, \quad (\text{S2.8})$$

and the outgoing wave can be expressed as

$$\Psi_{out} = \sum_m a_m \sum_{m'} S_{mm'} {}^k h_{m'}^{(+)}, \quad (\text{S2.9})$$

where the coefficients  $a_m$  are determined to yield a desired kind of incoming test wave,  $S_{mm'}$  denotes the transition amplitude for an incoming cylindrical wave  ${}^k h_m^{(-)}$  scattered into an outgoing one  ${}^k h_{m'}^{(+)}$ . This defines the  $S$ -matrix with  $m$  and  $m'$  covering all possible angular momentum channels. We thus have

$$\begin{aligned} \Psi(r, \theta) &= \sum_m a_m \left[ \begin{pmatrix} H_m^{(2)}(kr) \\ iH_{m+1}^{(2)}(kr)e^{i\theta} \end{pmatrix} e^{im\theta} + \sum_{m'} S_{mm'} \begin{pmatrix} H_{m'}^{(1)}(kr) \\ iH_{m'+1}^{(1)}(kr)e^{i\theta} \end{pmatrix} e^{im'\theta} \right], \\ &= \sum_m 2a_m \begin{pmatrix} J_m(kr) \\ iJ_{m+1}(kr)e^{i\theta} \end{pmatrix} e^{im\theta} + \sum_m a_m \sum_{m'} (S_{mm'} - \delta_{mm'}) \begin{pmatrix} H_{m'}^{(1)}(kr) \\ iH_{m'+1}^{(1)}(kr)e^{i\theta} \end{pmatrix} e^{im'\theta}. \end{aligned} \quad (\text{S2.10})$$

To be concrete, we assume the incident wave to be a plane wave given by

$$\chi_{k_{in}}(r, \theta) = \frac{1}{\sqrt{2}} \begin{pmatrix} 1 \\ e^{i\theta_{k_{in}}} \end{pmatrix} e^{i\mathbf{k}_{in} \cdot \mathbf{r}} = \frac{1}{\sqrt{2}} \begin{pmatrix} 1 \\ e^{i\theta'} \end{pmatrix} e^{ikr \cos(\theta - \theta')},$$

for massless Dirac fermions with positive energy  $E = \hbar v_F k$  and incident wavevector  $\mathbf{k}_{in} = k(\cos\theta', \sin\theta')$  that makes an angle  $\theta'$  with the  $x$  axis. This defines the incident propagating direction as shown in Fig. 1 in the main text. We have

$$\chi_{k_{in}} = \sum_m \frac{i^m e^{-im\theta'}}{\sqrt{2}} \begin{pmatrix} J_m(kr) \\ iJ_{m+1}(kr)e^{i\theta} \end{pmatrix} e^{im\theta}, \quad (\text{S2.11})$$

where the Jacobi-Anger expansion  $e^{iz \cos\theta} = \sum_m i^m J_m(z) e^{im\theta}$  has been used. Given the coefficients

$$a_m = a_m(\theta') = \frac{i^m e^{-im\theta'}}{2\sqrt{2}}, \quad (\text{S2.12})$$

and with the definition  $T_{mm'} \equiv S_{mm'} - \delta_{mm'}$ , we get

$$\Psi(r, \theta) = \chi_{k_{in}} + \sum_m a_m \sum_{m'} T_{mm'} \begin{pmatrix} H_{m'}^{(1)}(kr) \\ iH_{m'+1}^{(1)}(kr)e^{i\theta} \end{pmatrix} e^{im'\theta}. \quad (\text{S2.13})$$

Far away from the scatterer center, i.e.  $kr \gg 1$ , the asymptotic wavefunction can be written as

$$\lim_{kr \gg 1} \Psi = \chi_{k_{in}} + \frac{f(\theta, \theta')}{\sqrt{-ir}} \begin{pmatrix} 1 \\ e^{i\theta} \end{pmatrix} e^{ikr}, \quad (\text{S2.14})$$

where  $f$  is the scattering amplitude for two-dimensional massless Dirac fermions, which is related to the differential cross section through

$$\frac{d\sigma}{d\theta} \equiv \sigma(\theta, \theta') = |f(\theta, \theta')|^2, \quad (\text{S2.15a})$$

the total cross section through

$$\sigma_t(\theta') = \oint d\theta |f(\theta, \theta')|^2, \quad (\text{S2.15b})$$

the transport cross section through

$$\sigma_{tr}(\theta') = \oint d\theta (1 - \cos\theta) |f(\theta, \theta')|^2, \quad (\text{S2.15c})$$

and the skew cross section through

$$\sigma_{sk}(\theta') = \oint d\theta \sin\theta |f(\theta, \theta')|^2. \quad (\text{S2.15d})$$

It follows from Eqs. (S2.13) and (S2.14) that

$$\frac{f(\theta, \theta')}{\sqrt{-ir}} \begin{pmatrix} 1 \\ e^{i\theta} \end{pmatrix} e^{ikr} = \lim_{kr \gg 1} \sum_m a_m \sum_{m'} T_{mm'} \begin{pmatrix} H_{m'}^{(1)}(kr) \\ iH_{m'+1}^{(1)}(kr)e^{i\theta} \end{pmatrix} e^{im'\theta}.$$

Finally, we obtain

$$f(\theta, \theta') = i\sqrt{\frac{2}{\pi k}} \sum_{m'} \sum_m a_m(\theta') T_{mm'} (-i)^{m'} e^{im'\theta}. \quad (\text{S2.16})$$

Defining

$$f_l(\theta') = \sum_m a_m(\theta') T_{ml} (-i)^l = \sum_m a_m(\theta') (S_{ml} - \delta_{ml}) (-i)^l, \quad (\text{S2.17})$$

we rewrite the scattering amplitude as

$$f(\theta, \theta') = i\sqrt{\frac{2}{\pi k}} \sum_l f_l(\theta') e^{il\theta},$$

which, when substituted into Eqs. (S2.15a)-(S2.15d), leads to convenient summation forms of the various cross sections in terms of  $f_l(\theta')$  (and eventually the scattering matrix elements  $S_{ml}$ ) as

$$\sigma(\theta, \theta') = \frac{2}{\pi k} \left| \sum_l f_l(\theta') e^{il\theta} \right|^2 = \frac{2}{\pi k} \sum_{l,l'} \sum_{m,m'} a_m a_{m'}^* (S_{ml} - \delta_{ml}) (S_{m'l'}^* - \delta_{m'l'}) (-i)^{(l-l')\theta} e^{i(l-l')\theta}, \quad (\text{S2.18a})$$

$$\sigma_t(\theta') = \frac{4}{k} \sum_l |f_l(\theta')|^2 = \frac{4}{k} \sum_{m,m'} a_m (TT^\dagger)_{mm'} a_{m'}^*, \quad (\text{S2.18b})$$

$$\sigma_{tr}(\theta') = \sigma_t(\theta') - \frac{4}{k} \sum_l \Re[f_l f_{l+1}^*] = \sigma_t(\theta') - \frac{4}{k} \sum_{m,m'} \Re \left[ i a_m (T \hat{T}^\dagger)_{mm'} a_{m'}^* \right], \quad (\text{S2.18c})$$

and

$$\sigma_{sk}(\theta') = \frac{4}{k} \sum_l \Im[f_l f_{l+1}^*] = \frac{4}{k} \sum_{m,m'} \Im \left[ i a_m (T \hat{T}^\dagger)_{mm'} a_{m'}^* \right], \quad (\text{S2.18d})$$

where  $(\hat{T}^\dagger)_{lm'} \equiv (T^\dagger)_{l+1,m'} = T_{m',l+1}^*$ . All the scattering cross sections are functions of  $\theta'$  that defines the direction of the incident wave with respect to the  $x$  axis. Averaging over all the incident directions ( $\theta'$ ), we obtain the cross sections that are independent of the angle  $\theta'$  as

$$\bar{\sigma}_t = \frac{1}{2\pi} \oint d\theta' \sigma_t(\theta') = \frac{4}{k} \sum_{m,m'} \frac{1}{2\pi} \oint d\theta' a_m(\theta') (T \hat{T}^\dagger)_{mm'} a_{m'}^*(\theta') = \frac{1}{2k} \sum_{m,l} |T_{ml}|^2, \quad (\text{S2.19a})$$

$$\bar{\sigma}_{tr} = \bar{\sigma}_t - \frac{4}{k} \sum_{m,m'} \Re \left[ \frac{i}{2\pi} \oint d\theta' a_m(\theta') (T \hat{T}^\dagger)_{mm'} a_{m'}^*(\theta') \right] = \frac{1}{2k} \sum_{m,l} \left\{ |T_{ml}|^2 - \Re [iT_{ml} T_{m,l+1}^*] \right\}, \quad (\text{S2.19b})$$

and

$$\bar{\sigma}_{sk} = \frac{1}{2k} \sum_l \sum_{m,m'} \Im \left[ iT_{ml} (\hat{T}^\dagger)_{lm'} \delta_{mm'} \right] = \frac{1}{2k} \sum_{m,l} \Im [iT_{ml} T_{m,l+1}^*]. \quad (\text{S2.19c})$$

From the definition

$$T_{ml} = S_{ml} - \delta_{ml}, \quad (\text{i.e. } T = S - I),$$

we can calculate the characteristic cross sections once the scattering ( $S$ )-matrix is obtained.

In addition to the cross sections, associated with the  $S$ -matrix, another quantity of interest is the Wigner-Smith delay time [1, 2] defined as

$$\tau(E) = -i\hbar \text{Tr} \left[ S^\dagger \frac{\partial S}{\partial E} \right], \quad (\text{S2.20})$$

which characterizes the temporal aspects of the scattering process. The delay time is related to the density of states [3] through  $\rho(E) = \tau(E)/(2\pi\hbar)$ .

By definition, the transport cross section most appropriately characterizes the transport property, which determines the transport relaxation time  $\tau_{tr}$  according to the Fermi's golden rule with its reciprocal given by

$$\frac{1}{\tau_{tr}} = n_c v_F \sigma_{tr}, \quad (\text{S2.21})$$

where  $n_c$  is the concentration of identical scatterers that are assumed to be sufficiently dilute so that multiple scattering effects can be neglected. If the system dimension is larger than the mean-free path  $\mathcal{L} = v_F \tau_{tr}$ , from the semiclassical Boltzmann transport theory, we obtain the conductivity of the system as

$$\frac{G}{G_0} = k_F v_F \tau_{tr} = \frac{k}{n_c \sigma_{tr}}, \quad (\text{S2.22})$$

where  $G_0 = 2e^2/h$  is the conductance quantum.

### III. S-MATRIX FOR ECCENTRIC ANNULAR SHAPED (RING) SCATTERER

We perform an explicit calculation of the  $S$ -matrix for the scatterer of annular shape defined by two disks of different radii ( $R_1, R_2 < R_1$ ) with a finite relative displacement  $\xi$  of the disk centers, as shown in Fig. 1(a) in the main text. For convenience, we adopt the convention that the unprimed coordinates are defined by choosing the origin as the center of the larger disk  $O$  while the primed ones have their origin at the small disk center  $O'$ . Applying the standard  $S$ -matrix formalism, we obtain the wavefunction outside the eccentric annular scatterer, i.e.,  $|\mathbf{r}'| > R_1$ , in the unprimed polar coordinates  $\mathbf{r} = (r, \theta)$  as

$$\Psi^I(\mathbf{r}) = \sum_{m=-\infty}^{\infty} a_m^0 \left[ k_0 h_m^{(2)} + \sum_{m'=-\infty}^{\infty} S_{mm'} k_0 h_{m'}^{(1)} \right], \quad (\text{S3.23})$$

where  $S_{mm'}$  denotes the  $S$ -matrix elements in terms of the two given channels indexed by  $m$  and  $m'$ , respectively, and the coefficients  $a_m^0$  are chosen to yield a desired kind of incident test wave. Let  $k_0 \underline{h}_m^{(2)} \equiv a_m^0 k_0 h_m^{(2)}$  and  $\underline{S}_{mm'} \equiv a_m^0 S_{mm'}$ , and so

$$\Psi^I(\mathbf{r}) = \sum_{m=-\infty}^{\infty} \left[ k_0 \underline{h}_m^{(2)} + \sum_{m'=-\infty}^{\infty} \underline{S}_{mm'} k_0 h_{m'}^{(1)} \right]. \quad (\text{S3.24})$$

The wavefunction in the annular region ( $|\mathbf{r}'| > R_2$  and  $|\mathbf{r}'| < R_1$ ) can be expressed in the unprimed coordinates as

$$\Psi^{II}(\mathbf{r}) = \sum_{m=-\infty}^{\infty} \sum_{l=-\infty}^{\infty} {}^m a_l^1 \left[ k_1 h_l^{(2)} + \sum_{l'=-\infty}^{\infty} S_{ll'}^{od} k_1 h_{l'}^{(1)} \right], \quad (\text{S3.25})$$

where the resulting matrix  $S^{od} \equiv [S_{ll'}^{od}]$  characterizes the scattering from the off-centered small inner disk and is non-diagonal. Making use of the addition property of the Bessel functions, we obtain the following relation

$$S^{od} = U^{-1} S^{cd} U, \quad (\text{S3.26})$$

where the transformation matrices  $U = [U_{l\mu}] = [J_{\mu-l}(k_1 \xi)]$  and  $U^{-1} = [U_{ml}^{-1}] = [J_{m-l}(k_1 \xi)]$  are responsible for the eccentric displacement/deformation, and  $S^{cd} = [S_l^{cd} \delta_{ll'}]$  is the diagonal scattering matrix for the centered inner disk scatterer in the primed coordinates with its elements  $S_l^{cd}$  given by

$$S_l^{cd} = -\frac{\alpha_1 H_{l+1}^{(2)}(k_1 R_2) J_l(k_2 R_2) - \alpha_2 H_l^{(2)}(k_1 R_2) J_{l+1}(k_2 R_2)}{\alpha_1 H_{l+1}^{(1)}(k_1 R_2) J_l(k_2 R_2) - \alpha_2 H_l^{(1)}(k_1 R_2) J_{l+1}(k_2 R_2)}. \quad (\text{S3.27})$$

The  $S$ -matrix of the whole scatterer can thus be determined by the matching conditions at the outer boundary  $|\mathbf{r}'| = R_1$ . In Eqs. (S3.23) and (S3.25),  $k_{0,1} h_m^{(1,2)}$  denote the basic spinor waves consisting of the expanding basis indexed by the angular momentum in the polar coordinates and are explicitly given in Eq. (S5.44a). In particular, for a given incident spinor wave with angular momentum  $m$ , wavefunction matching for each momentum value  $j$  yields

$$a_m^0 H_m^{(2)}(k_0 R_1) \delta_{mj} + a_m^0 S_{mj} H_j^{(1)}(k_0 R_1) = {}^m a_j^1 H_j^{(2)}(k_1 R_1) + \sum_l {}^m a_l^1 S_{lj}^{od} H_j^{(1)}(k_1 R_1), \quad (\text{S3.28a})$$

$$i\alpha_0 \left[ a_m^0 H_{m+1}^{(2)}(k_0 R_1) \delta_{mj} + a_m^0 S_{mj} H_{j+1}^{(1)}(k_0 R_1) \right] = i\alpha_1 \left[ {}^m a_j^1 H_{j+1}^{(2)}(k_1 R_1) + \sum_l {}^m a_l^1 S_{lj}^{od} H_{j+1}^{(1)}(k_1 R_1) \right]. \quad (\text{S3.28b})$$

Defining matrices

$$\mathbb{X}^{(1,2)} = [H_m^{(1,2)}(k_0 R_1) \delta_{mj}], \quad \mathbb{Y}^{(1,2)} = [H_{m+1}^{(1,2)}(k_0 R_1) \delta_{mj}], \quad (\text{S3.29a})$$

and

$$\mathbf{x}^{(1,2)} = [H_m^{(1,2)}(k_1 R_1) \delta_{mj}], \quad \mathbf{y}^{(1,2)} = [H_{m+1}^{(1,2)}(k_1 R_1) \delta_{mj}], \quad (\text{S3.29b})$$

we can rewrite the above equations in the following compact form

$$\mathbb{A}^0 \mathbb{X}^{(2)} + \mathbb{A}^0 S \mathbb{X}^{(1)} = \mathbb{A} \mathbf{x}^{(2)} + \mathbb{A} S^{od} \mathbf{x}^{(1)}, \quad (\text{S3.30a})$$

$$\alpha_0 \left[ \mathbb{A}^0 \mathbb{Y}^{(2)} + \mathbb{A}^0 S \mathbb{Y}^{(1)} \right] = \alpha_1 \left[ \mathbb{A} \mathbf{y}^{(2)} + \mathbb{A} S^{od} \mathbf{y}^{(1)} \right], \quad (\text{S3.30b})$$

with the coefficient matrices  $\mathbb{A}^0 = [a_m^0 \delta_{mj}]$  and  $\mathbb{A} = [{}^m a_j^1]$ . Solving the above equations, we arrive at

$$S = - \frac{\mathbb{Y}^{(2)} - \alpha_0 \alpha_1 \mathbb{X}^{(2)} \mathbb{T}}{\mathbb{Y}^{(1)} - \alpha_0 \alpha_1 \mathbb{X}^{(1)} \mathbb{T}}, \quad (\text{S3.31})$$

where  $\mathbb{T} = \mathbb{F}^{-1} \mathbb{G}$  with the conventions  $\mathbb{F} = \mathbf{x}^{(2)} + S^{od} \mathbf{x}^{(1)}$ ,  $\mathbb{G} = \mathbf{y}^{(2)} + S^{od} \mathbf{y}^{(1)}$  and band indices  $\alpha_{0,1} = \pm 1$ . Substituting the  $S$ -matrix given in Eq. (S3.31) into Eq. (S3.30a), we obtain matrix  $\mathbb{A}$  consisting of the expansion coefficients  ${}^m a_l^1$  in the annular region as

$$\mathbb{A} = \frac{\mathbb{A}^0 \mathbb{X}^{(2)} + \mathbb{A}^0 S \mathbb{X}^{(1)}}{\mathbf{x}^{(2)} + S^{od} \mathbf{x}^{(1)}}. \quad (\text{S3.32})$$

#### IV. CALCULATION OF WAVEFUNCTIONS

Inside the inner disk region, i.e.,  $|r'| < R_2$ , the wavefunction in the primed polar coordinates  $\mathbf{r}' = (r', \theta')$  (with origin at the small disk center  $O'$ ) is

$$\tilde{\Psi}^{III}(r', \theta') = \sum_m \sum_l {}^m \tilde{b}_l \begin{pmatrix} J_l(k_2 r') \\ i s_2 J_{l+1}(k_2 r') e^{i\theta'} \end{pmatrix} e^{il\theta'}. \quad (\text{S4.33})$$

The expansion coefficients  ${}^m \tilde{b}_l$  can be determined by the matching condition at the inner boundary  $r' = |\mathbf{r} - \boldsymbol{\xi}| = R_2$  between  $\Psi^{(2)}(r', \theta')$  and  $\Psi^{(1)}(r, \theta)$ . To do so, it is convenient to reformulate the wavefunction inside the annular region in the primed coordinates. Using the relations

$$S_{ll'}^{od} = \sum_j J_{l-j} S_{jj}^{cd} J_{l'-j}, \quad (\text{S4.34a})$$

$$\delta_{ll'} = \sum_j J_{l-j} J_{l'-j}, \quad (\text{S4.34b})$$

and assuming  $l' = j + n$ , we have

$$\begin{aligned}
k_1 h_l^{(2)} + \sum_{l'=-\infty}^{\infty} S_{ll'}^{od} k_1 h_{l'}^{(1)} &\equiv \sum_{l'=-\infty}^{\infty} \left[ \delta_{ll'} k_1 h_{l'}^{(2)} + \sum_j J_{l-j} S_{jj}^{cd} J_{l'-j} k_1 h_{l'}^{(1)} \right], \\
&= \sum_{l'} \sum_j J_{l-j} \left[ J_{l'-j} k_1 h_{l'}^{(2)} + S_{jj}^{cd} J_{l'-j} k_1 h_{l'}^{(1)} \right], \\
&= \sum_j J_{l-j} \left[ \sum_n J_n k_1 h_{j+n}^{(2)} + S_{jj}^{cd} \sum_n J_n k_1 h_{j+n}^{(1)} \right].
\end{aligned} \tag{S4.35}$$

Making use of the Graf's addition theorem [4] for the Bessel functions  $Z_j \in \{J_j, H_j^{(1,2)}\}$ :

$$Z_j(kr') e^{ij\theta'} = \sum_n J_n(k\xi) Z_{j+n}(kr) e^{i(j+n)\theta},$$

we can rewrite the Eq. (S4.35) in the primed coordinates as

$$k_1 h_l^{(2)} + \sum_{l'=-\infty}^{\infty} S_{ll'}^{od} k_1 h_{l'}^{(1)} = \sum_j J_{l-j} \left[ k_1 \tilde{h}_j^{(2)} + S_{jj}^{cd} k_1 \tilde{h}_j^{(1)} \right], \tag{S4.36}$$

where

$$k_1 \tilde{h}_j^{(1,2)} = \begin{pmatrix} H_j^{(1,2)}(k_1 r') \\ i\alpha_1 H_{j+1}^{(1,2)}(k_1 r') e^{i\theta'} \end{pmatrix} e^{ij\theta'}. \tag{S4.37}$$

Substituting this expression into Eq. (S3.25), we obtain the wavefunction for the annular region in the primed coordinates as

$$\tilde{\Psi}^H(r', \theta') = \sum_m \sum_l \sum_j m a_l^1 J_{l-j} \left[ k_1 \tilde{h}_j^{(2)} + S_{jj}^{cd} k_1 \tilde{h}_j^{(1)} \right] = \sum_m \sum_l m \tilde{a}_l^1 \left[ k_1 \tilde{h}_l^{(2)} + S_{ll}^{cd} k_1 \tilde{h}_l^{(1)} \right], \tag{S4.38}$$

where

$$m \tilde{a}_l^1 = \sum_j m a_j^1 J_{j-l}(k_1 \xi). \tag{S4.39}$$

Imposing the continuity of the wavefunction at  $r' = R_2$ , we get

$$m \tilde{b}_l = m \tilde{a}_l^1 \frac{H_l^{(2)}(k_1 R_2) + S_{ll}^{cd} H_l^{(1)}(k_1 R_2)}{J_l(k_2 R_2)}. \tag{S4.40}$$

With the expansion coefficients  $m a_l^1$ ,  $m \tilde{a}_l^1$ , and  $m \tilde{b}_l$  so determined and the scattering matrices  $S, S^{od}, S^{cd}$  obtained in the relevant regions via Eqs. (S3.32, S4.39, S4.40) and Eqs. (S3.31, S3.26, S3.27), respectively, we can calculate the wavefunctions accordingly, which together give the full wavefunction in the entire space.

## V. IDEAL CENTRIC CASE: ANALYTIC RESULTS

For the centric case, i.e.,  $\xi = 0$ , we can obtain the analytic solutions of the scattering problem via the standard technique of partial wave decomposition. In particular, due to the circular rotational

symmetry and hence conservation of the total angular momentum, the partial waves outside the annular scatterer ( $r > R_2$ ) can be written as

$$\Psi_m^I = k_0 h_m^{(2)} + S_m k_0 h_m^{(1)}. \quad (\text{S5.41})$$

Inside the annular region  $R_1 < r < R_2$ , the waves are

$$\Psi_m^{II} = A_m \left[ k_1 h_m^{(2)} + S_m^{cd} k_1 h_m^{(1)} \right] \quad (\text{S5.42})$$

and

$$\Psi_m^{III} = B_m k_2 \chi_m, \quad (\text{S5.43})$$

in the inner disk region  $r < R_2$ , where  $[k_0, k_1, k_2] = [|E_0|, |E_0 - V_1|, |E_0 - V_2|] / \hbar v$ ,

$$k_{0,1} h_m^{(1,2)} = \begin{pmatrix} H_m^{(1,2)}(k_{0,1}r) \\ i\alpha_{0,1} H_{m+1}^{(1,2)}(k_{0,1}r) e^{i\theta} \end{pmatrix} e^{im\theta}, \quad (\text{S5.44a})$$

and

$$\chi_m = \begin{pmatrix} J_m(k_2r) \\ i\alpha_2 J_{m+1}(k_2r) e^{i\theta} \end{pmatrix} e^{im\theta}, \quad (\text{S5.44b})$$

with  $\alpha_{0,1,2} = \pm 1$  being the band index defined as the signs of  $E_0, (E_0 - V_{1,2})$ , respectively, and  $m = 0, \pm 1, \pm 2, \dots$  denote the orbital angular momentum. The scattering amplitudes  $S_m, S_m^{cd}$  and the expansion coefficients  $A_m, B_m$  can be determined from the boundary conditions  $\Psi_m^I(R_1, \theta) = \Psi_m^{II}(R_1, \theta); \Psi_m^{II}(R_2, \theta) = \Psi_m^{III}(R_2, \theta)$ , leading to the following linear matrix equation

$$\begin{pmatrix} H_m^{(2)}(k_1 R_2) & -J_m(k_2 R_2) & H_m^{(1)}(k_1 R_2) & 0 \\ \alpha_1 H_{m+1}^{(2)}(k_1 R_2) & -\alpha_2 J_{m+1}(k_2 R_2) & \alpha_1 H_{m+1}^{(1)}(k_1 R_2) & 0 \\ H_m^{(2)}(k_1 R_1) & 0 & H_m^{(1)}(k_1 R_1) & -H_m^{(1)}(k_0 R_1) \\ \alpha_1 H_{m+1}^{(2)}(k_1 R_1) & 0 & \alpha_1 H_{m+1}^{(1)}(k_1 R_1) & -\alpha_0 H_{m+1}^{(1)}(k_0 R_1) \end{pmatrix} \begin{pmatrix} A_m \\ B_m \\ C_m \\ S_m \end{pmatrix} = \begin{pmatrix} 0 \\ 0 \\ H_m^{(2)}(k_0 R_1) \\ \alpha_0 H_{m+1}^{(2)}(k_0 R_1) \end{pmatrix}, \quad (\text{S5.45})$$

where  $C_m \equiv A_m S_m^{cd}$ . From the standard quantum scattering theory, we have that  $S_m$  is an element of the  $S$ -matrix for the concentric circular scatterer, which is diagonal in the basis of angular momentum states  $m$ . Solving Eq. (S5.45), we obtain the coefficients as

$$A_m = \frac{H_m^{(2)}(k_0 R_1) + H_m^{(1)}(k_0 R_1) S_m}{H_m^{(2)}(k_1 R_1) + H_m^{(1)}(k_1 R_1) S_m^{cd}}; \quad B_m = A_m \frac{H_m^{(2)}(k_1 R_2) + H_m^{(1)}(k_1 R_2) S_m^{cd}}{J_m(k_2 R_2)}, \quad (\text{S5.46a})$$

while the scattering amplitudes for the whole scatterer are given by

$$S_m = -\frac{\alpha_0 x_m H_{m+1}^{(2)}(k_0 R_1) - \alpha_1 y_m H_m^{(2)}(k_0 R_1)}{\alpha_0 x_m H_{m+1}^{(1)}(k_0 R_1) - \alpha_1 y_m H_m^{(1)}(k_0 R_1)}, \quad (\text{S5.46b})$$

where  $x_m = H_m^{(2)}(k_1 R_1) + H_m^{(1)}(k_1 R_1) S_m^{cd}$  and  $y_m = H_{m+1}^{(2)}(k_1 R_1) + H_{m+1}^{(1)}(k_1 R_1) S_m^{cd}$  with  $S_m^{cd}$  given by Eq. (S3.27).

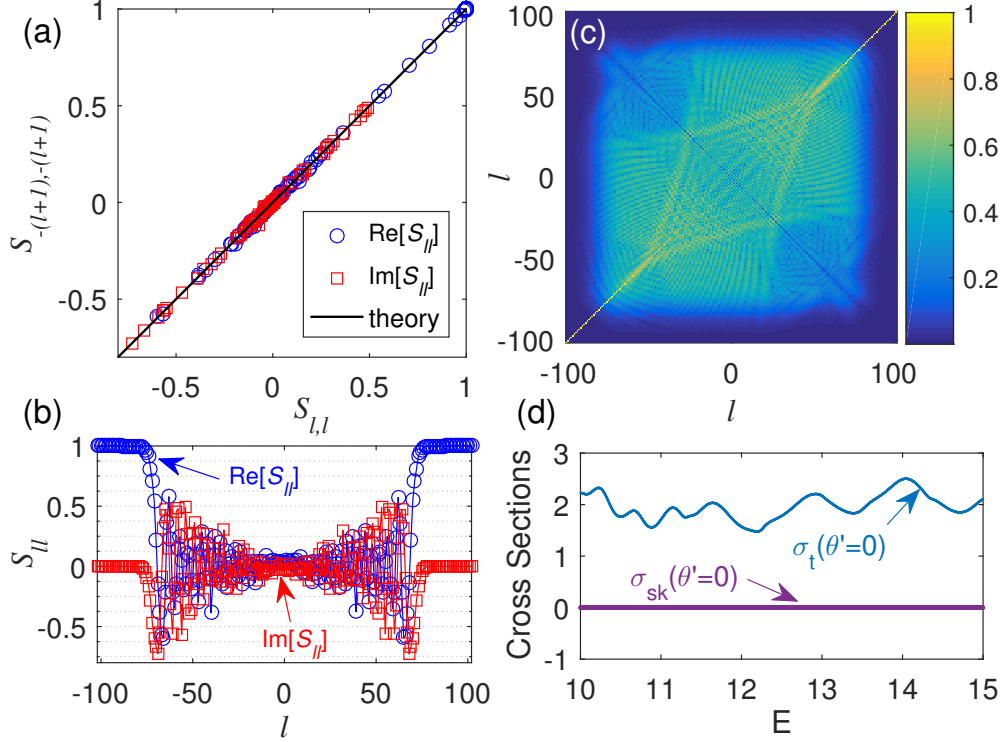


FIG. S1. **Validation of the  $S$ -matrix approach through the closed-form analytic constraints imposed by the symmetry of the system.** (a) Plot of the diagonal elements  $S_{-(l+1),-(l+1)}$  versus  $S_{l,l}$ , where the thick black line is the theoretical prediction of Eq. (S6.49), (b) real and imaginary parts of  $S_{ll}$ , (c) false color-coded map of the magnitudes of the full scattering matrix elements with a proper cut-off at  $l = \pm 102$  (the scale bar shows the fourth root of magnitudes  $|S_{ll}|$ ); (d) the skew cross section  $\sigma_{sk}$  (purple line) and the total cross section  $\sigma_t$  (light blue curve) as a function of the energy for incident waves propagating parallel to the symmetry axis, where the vanishing skew (asymmetric) scattering, i.e.,  $\sigma_{sk} \equiv 0$ , is consistent with the prediction of Eq. (S6.51). Parameters adopted for (a)-(c) are  $E = 70$ ,  $R_2/R_1 = 0.6$ ,  $\xi = 0.3$ ,  $v_1 = -140$ , and  $v_2 = 0$ . For (d), the parameters are  $R_2/R_1 = 0.6$ ,  $\xi = 0.3$ ,  $v_1 = -10$  and  $v_2 = 40$ .

## VI. VALIDATION OF THE $S$ -MATRIX APPROACH

### A. Symmetry constraints

In spite of the lack of circular rotational symmetry, the system possesses a mirror (parity) symmetry, which imposes certain constraints on the  $S$ -matrix and leads to vanishing of skew (asymmetric) scattering provided that the incident wave propagates along the axis of the symmetry. In particular, for the configuration shown in Fig. 1(a) in the main text, for spinor scattering we can explicitly write the representation of the parity symmetry operation as  $\mathcal{P}_x = \sigma_x \mathcal{R}_y$ , with  $\mathcal{R}_y$ , which is the reflection operator that acts in the physical (position) space with respect to the  $x$  axis via the operations  $x \rightarrow x (k_x \rightarrow k_x)$  and  $y \rightarrow -y (k_y \rightarrow -k_y, \theta \rightarrow -\theta)$ . As such, the system is invariant under parity, stipulating the relation  $\mathcal{P}_x H \mathcal{P}_x^{-1} = H$  so that  $\mathcal{P}_x \Psi$  is still a state of the system with the same energy. Under the operation of  $\mathcal{P}_x$ , the spinor cylindrical wave  $^k h_m^{(1,2)}$  of given orbital angular

momentum  $m$  (corresponding to total angular momentum  $L = m + 1/2$ ) can be transformed as

$$\begin{aligned} \mathcal{P}_x^k h_m^{(1,2)} &= i\sigma_x \mathcal{R}_y \left( \begin{array}{c} H_m^{(1,2)}(kr) \\ i\alpha H_{m+1}^{(1,2)}(kr) e^{i\theta} \end{array} \right) e^{im\theta} = (-)^{m+1} i\alpha \left( \begin{array}{c} H_{-(m+1)}^{(1,2)}(kr) \\ i\alpha H_{-m}^{(1,2)}(kr) e^{i\theta} \end{array} \right) e^{-i(m+1)\theta}, \\ &= (-)^{m+1} i\alpha^k h_{-(m+1)}^{(1,2)}. \end{aligned} \quad (\text{S6.47})$$

Applying this relation to the resulting state  $\Psi^{(0)}$  given in Eq. (S3.23), we obtain

$$\begin{aligned} \mathcal{P}_x \Psi^l &= \sum_m \mathcal{P}_x a_m^0 \mathcal{P}_x^{-1} \mathcal{P}_x \Psi_m = \sum_{m=-\infty}^{\infty} \mathcal{P}_x a_m^0 \mathcal{P}_x^{-1} \mathcal{P}_x \left[ k_0 h_m^{(2)} + \sum_{m'=-\infty}^{\infty} S_{mm'} k_0 h_{m'}^{(1)} \right], \\ &= \sum_{m=-\infty}^{\infty} \bar{a}_m^0 (-)^{m+1} i\alpha_0 \left[ k_0 h_{-(m+1)}^{(2)} + \sum_{m'=-\infty}^{\infty} \mathcal{P}_x S_{mm'} \mathcal{P}_x^{-1} (-)^{m'-m} k_0 h_{-(m'+1)}^{(1)} \right], \\ &\equiv \sum_n c_n^0 \Psi_n = \sum_{n=-\infty}^{\infty} c_n^0 \left[ k_0 h_n^{(2)} + \sum_{n'=-\infty}^{\infty} S_{nn'} k_0 h_{n'}^{(1)} \right], \end{aligned} \quad (\text{S6.48})$$

with deduced identities  $n \equiv -(m+1)$ ,  $n' \equiv -(m'+1)$ ,  $c_n^0 \equiv \bar{a}_m^0 (-)^{m+1} i\alpha_0 = \mathcal{P}_x a_m^0 \mathcal{P}_x^{-1} (-)^{m+1} i\alpha_0$ . We thus have

$$S_{nn'} \equiv S_{-(m+1), -(m'+1)} = \mathcal{P}_x S_{mm'} \mathcal{P}_x^{-1} (-)^{m'-m} = (-)^{m'-m} S_{mm'}. \quad (\text{S6.49})$$

In particular, for  $m = m'$ , i.e., the diagonal elements, we have  $S_{mm} = S_{-(m+1), -(m+1)}$ . Under such constrains and using the definition of  $f_l(\theta')$  given in Eq. (S2.17), we have

$$\begin{aligned} f_l(\theta') &= \sum_m a_m(\theta') (S_{ml} - \delta_{ml}) (-i)^l, \\ &= \sum_m \frac{i^m e^{-im\theta'}}{2\sqrt{2}} \left[ (-)^{m-l} S_{-(m+1), -(l+1)} - \delta_{-(m+1), -(l+1)} \right] (-i)^{2l+1} (-i)^{-(l+1)}, \\ &= e^{i\theta'} \sum_m \frac{i^{-(m+1)} e^{-i(m+1)\theta'}}{2\sqrt{2}} \left[ S_{-(m+1), -(l+1)} - \delta_{-(m+1), -(l+1)} \right] (-i)^{-(l+1)}, \\ &= e^{i\theta'} \sum_{m'} a_{m'}(-\theta') \left[ S_{m', -(l+1)} - \delta_{m', -(l+1)} \right] (-i)^{-(l+1)} \equiv e^{i\theta'} f_{-(l+1)}(-\theta'). \end{aligned} \quad (\text{S6.50})$$

For  $\theta' = 0$  ( $\pi$ ), i.e., when the incident wave propagates parallel (anti-parallel) to the axis of the mirror symmetry, we obtain  $f_l = \pm f_{-(l+1)}$ , based on which we can rewrite the skew cross section in Eq. (S2.18d) as

$$\begin{aligned} \sigma_{sk} |_{\theta'=0(\pi)} &= \frac{4}{k} \sum_l \Im [f_l f_{l+1}^*] = \frac{4}{k} \Im \left\{ |f_0|^2 + \sum_{l=0}^{\infty} \left[ f_l f_{l+1}^* + f_{-(l+1)} f_{-(l+1)}^* \right] \right\}, \\ &= \frac{4}{k} \Im \left[ |f_0|^2 + \sum_{l=0}^{\infty} 2\Re(f_l f_{l+1}^*) \right] \equiv 0. \end{aligned} \quad (\text{S6.51})$$

These basic symmetry induced, exact constrains given by the closed forms in Eqs. (S6.49) and (S6.51) can serve as benchmarks for validating the  $S$ -matrix approach. Note that, while theoretically the dimension of the  $S$ -matrix is infinite, in practice a finite truncation is needed for a given

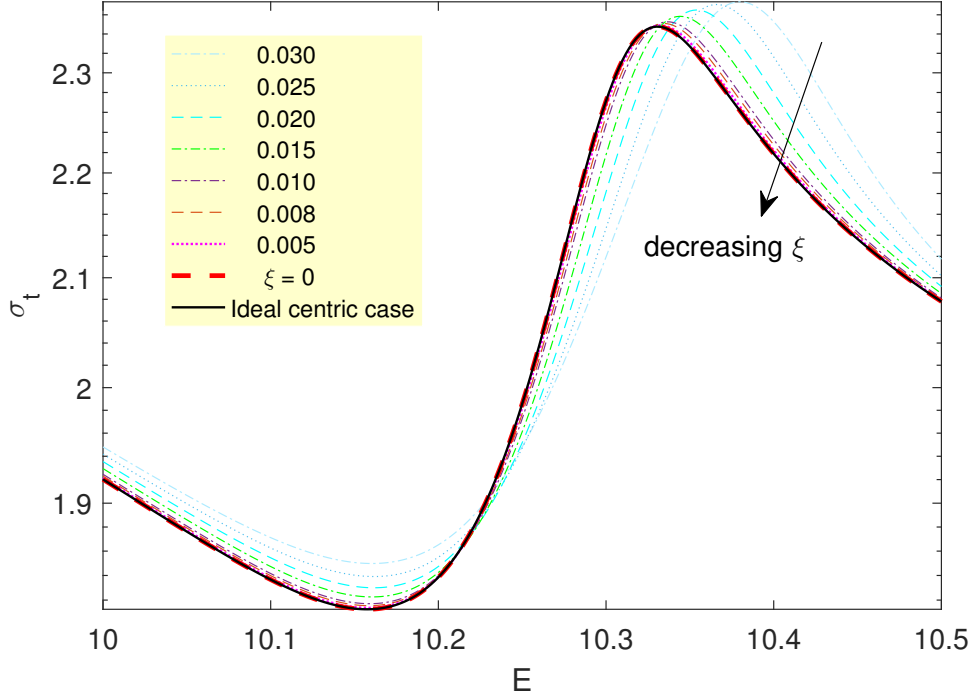


FIG. S2. **Validate the  $S$  matrix approach by showing the convergence to the integrable case.** For the case of classically integrable dynamics, the agreement between the theoretically predicted cross section values [the black curve calculated from Eqs. (S5.46b)] and the numerical results as  $\xi$  approaches zero. Parameters are  $R_2/R_1 = 0.6$ ,  $v_1 = -10$ , and  $v_2 = 40$ .

energy  $E$  since channels with higher angular momenta  $l \gg ER/\hbar v$  cannot be excited effectively and thus have negligible contribution to the scattering process. Representative results are shown in Fig. S1. We obtain a good agreement between the theoretical prediction and the simulation results from properly truncated  $S$ -matrices.

### B. The case of $\xi \rightarrow 0$

Numerically, it is straightforward to validate the  $S$ -matrix approach indirectly by evaluating the convergence of the value of the cross section to the theoretical value for the limiting case of  $\xi \rightarrow 0$  at which the classical dynamics are integrable. As shown in Fig. S2, a good agreement is achieved for  $\xi < 0.01$ .

## VII. FULL DATA SET FOR THE PLOT FIG. 2(C) IN THE MAIN TEXT

Figure S3(a) shows the spin polarization versus  $\xi$  and the Fermi energy  $E$ , where the deep sky-blue regions in the energy domain indicating higher values of spin polarization become extended as  $\xi$  is increased and exceeds the value of 0.2. Figure S3(b) shows the average spin conductivities versus  $\xi$ , where the conductivity for the spin up population is a decreasing function of  $\xi$  but that for

the spin down state is essentially constant. Thus, on average the spin up particles undergo significantly stronger backward scattering as compared with the spin down particles, generating a severe spin imbalance (e.g., for  $\xi = 0.3$ ) and consequently, significantly enhanced spin polarization. To appreciate the role of deformation played in generating a strong Dirac quantum chimera state, we calculate the average differential cross section  $\Delta\bar{\sigma}_{diff} \equiv (E_2 - E_1)^{-1} \int_{E_1}^{E_2} (\sigma_{diff}^\uparrow - \sigma_{diff}^\downarrow) dE$  versus the backward scattering angle  $\theta$  for two cases:  $\xi = 0$  and  $\xi = 0.3$ , as shown in Fig. S3(c). A schematic illustration of the generation of spin polarization is shown in Fig. S3(d).

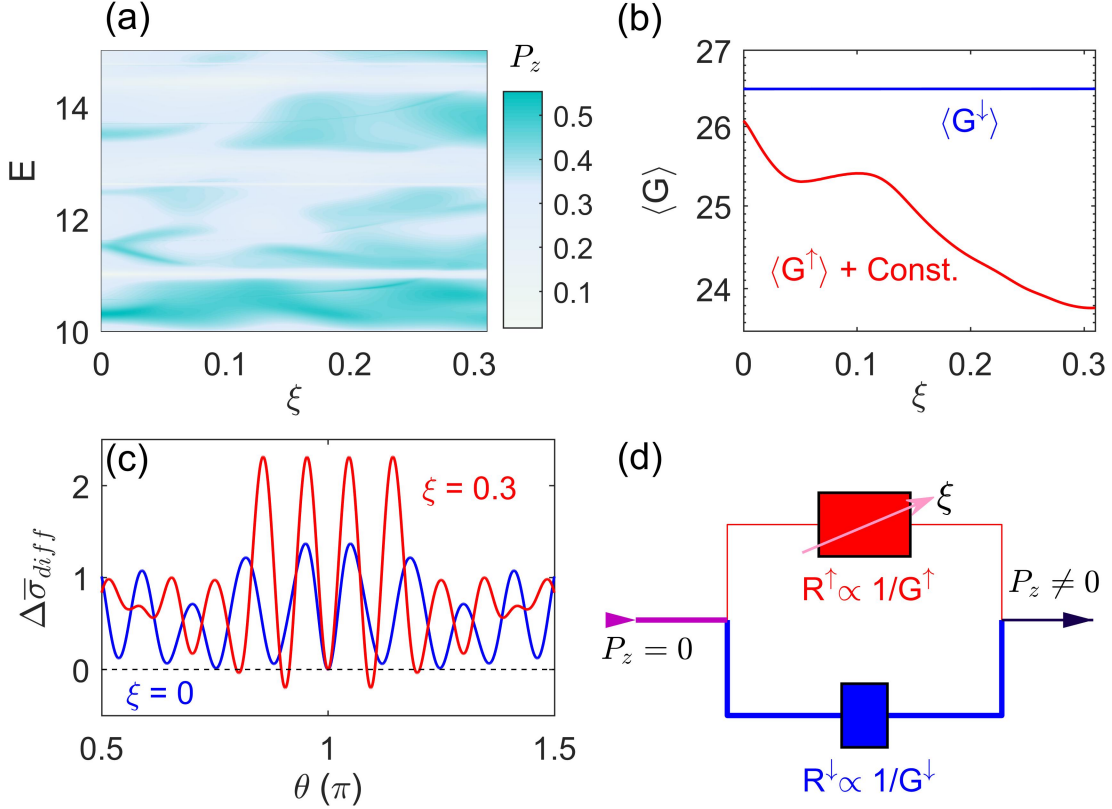


FIG. S3. **Spin polarization enhancement as a result of Dirac quantum chimera.** (a) Color-coded map of spin polarization  $P_z$  as a function of energy  $E$  and eccentricity  $\xi$ , (b) spin conductivities averaged over a given Fermi energy range versus  $\xi$ , where the red curve is vertically shifted by an arbitrary amount for better visualization, (c) illustration of a chaos rendered spin rheostat tuned by  $\xi$ , and (d) a schematic illustration of the generation of spin polarization.

### VIII. FEASIBILITY OF EXPERIMENTAL IMPLEMENTATION

In general, the emergence of a Dirac chimera relies on the optical like behavior of Dirac electrons and Dirac cone splitting, which can be realized in current experimental systems of graphene. In particular, given the graphene lattice constant and typical values of the Fermi wavelength (e.g.,  $\lambda_F \sim 20\text{nm}$ ), a Dirac description of the step potential requires the length scale characterizing the junction sharpness to be  $d \sim 1\text{nm}$ , which has been recently achieved experimentally for a circular

junction geometry [5]. The size of the junction can be tuned to the micrometer scale ( $\gg \lambda_F$ ), validating the short wavelength approximation [6]. Furthermore, the experimentally achievable strength of the exchange potential for graphene is strong enough to enable Dirac cone splitting at the room temperature [7], providing a base for experimentally observing the predicted Dirac quantum chimera.

---

- [1] E. P. Wigner, Phys. Rev. **98**, 145 (1955).
- [2] F. T. Smith, Phys. Rev. **118**, 349 (1960).
- [3] H. Schomerus, M. Marciani, and C. W. J. Beenakker, Phys. Rev. Lett. **114**, 166803 (2015).
- [4] D. Zwillinger, *Table of Integrals, Series, and Products* (Elsevier Science, 2014).
- [5] C. Gutierrez, L. Brown, C.-J. Kim, J. Park, and A. N. Pasupathy, Nat. Phys. **12**, 1069 (2016).
- [6] Y. Jiang, J. Mao, D. Moldovan, M. R. Masir, G. Li, K. Watanabe, T. Taniguchi, F. M. Peeters, and E. Y. Andrei, Nat. Nanotech. **12**, 1045 (2017).
- [7] P. Wei, S.-W. Lee, F. Lemaitre, L. Pinel, D. Cutaia, W.-J. Cha, F. Katmis, Y. Zhu, D. Heiman, J. Hone, and J. S. M. C.-T. Chen, Nat. Mater. **15**, 711 (2016).